

Atmospheric Newtonian noise modeling for third-generation gravitational wave detectors

D. Brundu,^{1,*} M. Cadoni,^{1,2,†} M. Oi,^{1,2,‡} P. Olla,^{1,3,§} and A. P. Sanna^{1,2,¶}

¹*I.N.F.N., Sezione di Cagliari, Cittadella Universitaria, 09042 Monserrato, Italy*

²*Dipartimento di Fisica, Università di Cagliari, Cittadella Universitaria, 09042 Monserrato, Italy*

³*ISAC-CNR, Sezione di Cagliari, Cittadella Universitaria, 09042 Monserrato, Italy*

The sensitivity and the frequency bandwidth of third-generation gravitational-wave (GW) detectors are such that the Newtonian noise (NN) signals produced by atmospheric turbulence could become relevant. We build models for atmospheric NN that take into account finite correlation times and inhomogeneity along the vertical direction, and are therefore accurate enough to represent a reliable reference tool for evaluating this kind of noise. We compute the NN spectral density from our models and compare it with the expected sensitivity curve of the Einstein Telescope (ET) with the xylophone design. The noise signal decays exponentially for small values of the frequency and the detector's depth, followed by a power-law for large values of the parameters. We find that, when the detector is built at the earth's surface, the NN contribution in the low-frequency band is above the ET sensitivity curve for strong wind. Building the detector underground is sufficient to push the noise signal under the ET sensitivity curve, but the decrement is close to marginal for strong wind. In light of the slow decay with depth of the NN, building the detector underground could be only partially effective as passive noise mitigation.

I. INTRODUCTION

The first direct observation of gravitational waves (GW) performed in the last years by the LIGO–Virgo collaboration [1–10] represents a milestone for fundamental physics and astrophysics. The direct detection of the GW signals generated by coalescing objects like neutron-stars or black-hole binaries has not only provided a striking confirmation of Einstein's General Relativity in the strong-field regime, but has also started the new era of multi-messenger astrophysics. The international network of second-generation GW detectors has been further enhanced with the joining of the KAGRA detector in 2020 [11–13]. The currently operating GW detectors use extremely sensitive Michelson interferometers and have a sensitivity band ranging from 10 Hz to 10 kHz.

Third-generation GW detectors like the Einstein Telescope (ET) [14] and Cosmic Explorer (CE) [15] have been proposed to fully open the emerging field of GW astrophysics and cosmology [16, 17]. Their goal is to improve the sensitivity by a factor of 10 and push the observation band down to 1 Hz. These improvements are motivated by numerous scientific reasons [17]. Black-hole mergers could be observed at higher redshift and mass; the inspiral phase could be detected earlier allowing for a better multi-messenger investigation of the source; possible quantum gravity effects, e.g. quantum hair(s) for black holes, could be detected in the ringdown phase. These are just a few examples of the scientific relevance of third-generation GW detectors.

Improvements in sensitivity and frequency bandwidth pose formidable challenges due to the impact of various noise sources. This is not only because the enhancement of the sensitivity of a factor of 10 may push the latter down close to the noise floor, but also because we need better modeling of noise in the lowest part of the frequency band. In fact, at few Hz, the major limitations are expected to come from the gravitational fluctuations, also called gravitational gradient noise or Newtonian Noise (NN) [18, 19]. NN has two main contributions coming from seismic fields and atmospheric perturbations. While detailed estimations of seismic NN have been performed—also by modeling seismic sources (for a comprehensive review, see, e.g. Ref. [18] and references therein)—atmospheric NN is instead poorly understood. Our understanding of the atmospheric contribution to the NN in GW detectors has, until now, been essentially based on the works of Saulson [20] and Creighton [21] (see also Ref. [22] for an analysis of the contributions coming from pressure fluctuations produced in turbulent flow and Ref. [22] for an analysis of acoustic NN). Saulson considered the effect of acoustic pressure waves. Conversely, Creighton investigated the contributions to NN of temperature perturbations, transient atmospheric shocks and sound waves generated by colliding objects. This lack of interest in the atmospheric contributions to the NN is motivated by the fact that estimations predicting NN in the 10 Hz region are several orders of magnitudes below the sensitivity curve of second-generation GW interferometers [18].

The situation changes drastically when one considers third-generation GW detectors. In this case, the NN prediction derived from modeling wind-advected temperature fluctuations, which are the dominant sources of atmospheric density fluctuations, cannot be extended below 10 Hz without modifying the models [21]. This is because the two basic assumptions adopted in [18, 20, 21]

* davide.brundu@ca.infn.it

† mariano.cadoni@ca.infn.it

‡ mauro.oi@ca.infn.it

§ olla@dsf.unica.it

¶ asanna@dsf.unica.it

for the estimation of NN generated by temperature fluctuations, namely, the quasi-static approximation and the homogeneity and isotropy hypothesis, are expected to fail in that frequency band.

A second crucial issue is that some third-generation GW detectors are planned to be built underground. Although it is generally qualitatively true that underground construction of the interferometers will represent passive mitigation of both seismic and atmospheric NN, quantitative results for the dependence of the noise level on the detector depth are not presently available. Again, this is because atmospheric NN modeling in the past was oriented towards second-generation GW-detectors, i.e. detectors built on the earth's surface.

The main purpose of this paper is to improve the modeling of NN generated by wind-advected temperature fluctuations, to make it a reliable reference tool for the evaluation of NN for third-generation GW detectors. This is going to be a necessary ingredient not only for a general preliminary estimation of the noise, but also for the successive, detailed evaluation of NN by numerical simulation of atmospheric flows in realistic conditions. This is mainly because current atmospheric codes have a grid scale that is typically well above that of the fluctuations expected to contribute to NN.

We will improve the quasi-static and homogeneous models of [21] by working in two different directions. Firstly, we will go beyond the former approximation by building models in which the NN generated by the decay of the vortices is taken into account. Secondly, we will fully take into account the fact that atmospheric turbulence is strongly inhomogeneous along the vertical direction, and therefore it cannot be modeled *a priori* within a homogeneous-isotropic (HI) turbulence framework. We will find that, whenever vortex time-decay dominates over the wind-advection component, the NN power spectra are characterized by a power-law behavior. This result is only weakly dependent on the specific form of the time correlations of the turbulence, except for its scaling properties. This is fully expected given the multi-scale behavior of turbulent phenomena. On the other hand, the power-law regime of NN spectra has not been previously found in HI models of frozen turbulence [21], and its possible impact on GW detectors was therefore completely overlooked.

We will then apply the results of our models to assess the impact of temperature-fluctuations-induced NN on the planned ET detector. For this purpose, we will compare the numerical NN power spectrum obtained from our models with the expected sensitivity curve of the ET with the xylophone design (ET-D configuration). We will also discuss the dependence of the power spectrum on the physical parameters of our model, putting a particular emphasis on the dependence on the detector depth r_0 . In the frequency range of interest, we will find that the noise, as a function of r_0 , decays exponentially for small values of this parameter. A $1/r_0^2$ scaling sets in at relatively large values of r_0 . This scaling behavior turns out to

be generally true whenever the effect of wind advection is negligible and r_0 is large. This implies that building the detector underground could not provide sufficient passive mitigation of atmospheric NN.

The structure of the paper is as follows. In Section II we discuss in general terms the modeling of NN from atmospheric temperature fluctuations beyond the quasi-static approximation. In Section III we briefly discuss the main features of turbulence in the planetary boundary layer (PBL). We model the NN generated by wind-advected HI turbulence in Section IV. In Section V we build a realistic model for NN generated by turbulence in the PBL. In Section VI we present the power spectra derived from our models, for selected values of the parameters, compare them with the ET-D sensitivity curve and discuss our results. In Section VII we draw our conclusions. We leave technical details to the appendices.

II. ATMOSPHERIC NOISE FROM TEMPERATURE FLUCTUATION

Density perturbations $\delta\rho(\mathbf{r}, t)$ in the air caused by temperature fluctuations $\delta T(\mathbf{r}, t) \equiv \tilde{T}(\mathbf{r}, t)$ are a major source of atmospheric NN for GW detectors. The heat in the atmosphere generates convective turbulence, mixing pockets of cold and warm air at all length-scales down to the millimeter. Indicating with \bar{T} and $\bar{\rho}$ the mean temperature and density of air, respectively, from the ideal gas law at constant temperature we get $\delta\rho(\mathbf{r}, t) = -(\bar{\rho}/\bar{T})\tilde{T}(\mathbf{r}, t)$. Density perturbations generated by temperature fluctuations are typically several orders of magnitude larger than those generated by pressure perturbations, which disperse in the atmosphere in the form of infrasound waves. The gravitational acceleration perturbation $\delta\mathbf{a}(\mathbf{r}_0, t)$ produced on the test-mass of the detector located at \mathbf{r}_0 at time t is given by

$$\delta\mathbf{a}(\mathbf{r}_0, t) = -\alpha \int dV \frac{\tilde{T}(\mathbf{r}, t)}{|\mathbf{r} - \mathbf{r}_0|^3} (\mathbf{r} - \mathbf{r}_0), \quad (1)$$

where $\alpha = G\bar{\rho}/\bar{T}$ is the conversion factor from temperature to acceleration fluctuations in the detector. The acceleration fluctuation given by Eq. (1) must then be projected onto the detector-arm direction in order to obtain the strain.

Physically, the time variation of the acceleration $\delta\mathbf{a}(\mathbf{r}_0, t)$ is the result of two different effects: the decay of vortices and their transport by the wind with average velocity \mathbf{U} past the detector. The approach adopted in [18, 21], which approximates turbulence as a frozen field, is based on the hypothesis that the vortex decay time-scale (identified with the eddy turnover time) is much larger than the typical time spent by the vortex in the vicinity of the detector [21]. In this approximation, the main contribution to Eq. (1) is due to the effect of frozen temperature fluctuations transported by the wind near the detector. As explained in the introduction, it is commonly believed that this approximation breaks down at

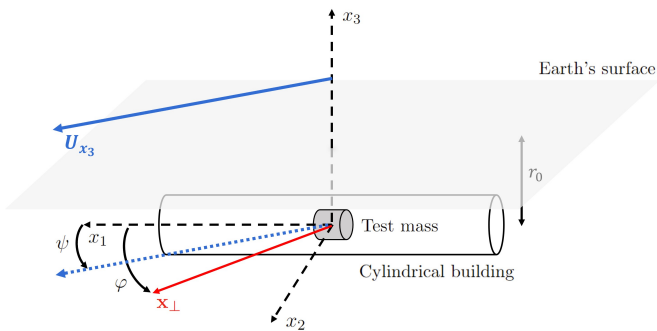


Figure 1. Schematic representation of the geometry of the system adopted to compute the Green functions. The system of cylindrical coordinates (x_\perp, φ, x_3) is highlighted, while $\mathbf{U}_{\mathbf{x}_3}$ refers to the direction of the wind, parallel to the earth's surface. The dotted blue arrow is the projection of the wind onto the plane of the test mass, while ψ is the angle between the detector arm, which is taken along x_1 , and the wind direction.

time-scales larger than 10 seconds [18, 21]. However, this is a rather intricate point, which deserves to be carefully analyzed. Indeed, the frozen turbulence limit has to be defined in terms of both the decay time of temperature correlations in the reference frame of the wind and the effective time the turbulent structure is perturbing the detector. We will discuss this issue in detail in Section IV A.

Direct calculation of the acceleration fluctuation from the temperature field using Eq. (1) is hopeless. The best we can do is to characterize the gravity gradient noise with its spectral density (power spectrum) $S_g(\omega, r_0)$

$$S_g(\omega, r_0) = \int d^3x d^3x' G_{\mathbf{k}}(\mathbf{x}, r_0) G_{\mathbf{k}}(\mathbf{x}', r_0) C_\omega^T(\mathbf{x}, \mathbf{x}') \quad (2)$$

where

$$C_\omega^T(\mathbf{x}, \mathbf{x}') = \int dt C^T(\mathbf{x}, \mathbf{x}'; t) e^{i\omega t}, \\ \equiv \int dt \langle \tilde{T}(\mathbf{x}, t) \tilde{T}(\mathbf{x}', 0) \rangle e^{i\omega t}, \quad (3)$$

and $G_{\mathbf{k}}(\mathbf{x}, r_0)$ is the spatial Green function. In the previous equations $\langle \tilde{T}(\mathbf{x}, t) \tilde{T}(\mathbf{x}', 0) \rangle$ is the autocorrelation of the temperature fluctuation field at two different points and at two different times. The stationarity of the random process implies this autocorrelation to be a function of the time difference. The specific form of the Green function $G_{\mathbf{k}}(\mathbf{x}, r_0)$, which we report in Appendix A, depends on both the geometry of the problem and the coordinate choice. The geometry of the system and the set of coordinates used to perform the calculations are sketched in Fig. 1.

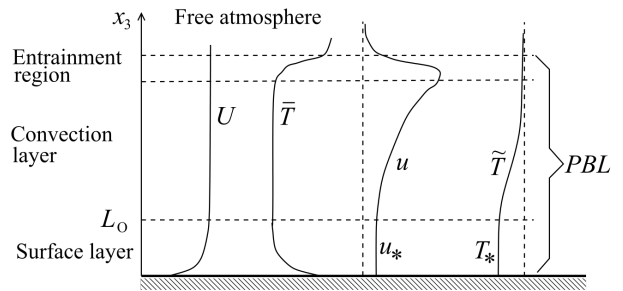


Figure 2. Portrait (not on scale) of the PBL structure. Vertical dashed lines indicate the zeros of the curves for turbulent velocity fluctuations u and temperature fluctuations \tilde{T} .

III. TURBULENCE IN THE PLANETARY BOUNDARY LAYER

Atmospheric turbulence is concentrated in the lowest portion of the troposphere, a region called the planetary boundary layer (PBL) [23]. The structure of the PBL is strongly dependent on the orography, the wind and weather conditions, and the hour in the day.

Let us consider the structure of the PBL on a typical sunny day—which means that the layer is unstably stratified—in the presence of strong wind. Under these conditions, the atmospheric turbulence contribution to NN is expected to be the maximum. For simplicity we consider the case of a horizontally uniform PBL developing over a plain region, and assume stationarity over the time-scales of interest.

The PBL can be subdivided into a surface layer in which mechanical stresses, originating from the wind interaction with the earth's surface, dominate the dynamics, and a convection layer in which stratification is dominant. A sketch of the PBL structure is shown in Fig. 2. In the surface layer, the mean wind speed $U = U_{x_3}$ is characterized by a logarithmic vertical profile [24]

$$U_{x_3} \simeq \frac{u_*}{\kappa} \ln(x_3/z_0), \quad (4)$$

where $\kappa = 0.4$ is a universal constant called the von Karman constant, u_* is the so-called friction velocity, which gives the velocity scale of the profile, and z_0 is an experimental parameter giving the dependence of the profile on the roughness of the terrain. In the case of a smooth surface $z_0 \simeq 0.1\nu/u_*$, where ν is the viscosity of the fluid. For Eq. (4) to be valid, it is necessary that $x_3 \gg z_0$. Values of the roughness length z_0 for different types of terrain are listed in Table I.

The friction velocity u_* gives the amplitude of the turbulent velocity fluctuations u in the surface layer. A similar parameter T_* can be introduced, giving the amplitude of the temperature fluctuations. Both u_* and T_* are constant in the surface layer. To characterize the strength of the wind, we shall use the mean wind speed at a reference height $x_3^{\text{ref}} = 10\text{ m}$: $U_{\text{ref}} \equiv U_{10\text{ m}}$.

At height x_3 , turbulent eddies are expected to be at

z_0 (m)	Terrain surface characteristics
1.0	city
0.8	forest
0.2	bushes
0.05	farmland (open appearance)
0.008	mown grass
0.005	bare soil (smooth)
0.0003	sand surfaces (smooth)

Table I. Schematics of terrain types and z_0 values [25].

most $\sim x_3$ in size, although they tend to be more elongated in the direction of the mean flow than in the vertical and spanwise directions. Similar considerations are valid for temperature fluctuations. This identifies a characteristic time-scale of fluctuations in the surface layer

$$\tau(x_3) \sim x_3/u_*. \quad (5)$$

We can compare the time-scale $\tau(x_3)$ with the time-scale of convection $\tau_{\text{conv}}(x_3) \sim [\bar{T}x_3/(gT_*)]^{1/2}$, where $g = 9.81 \text{ m/s}^2$ is the gravitational acceleration. The transition from the surface layer to the convection-dominated part of the PBL takes place for $\tau(x_3) \sim \tau_{\text{conv}}(x_3)$, which defines (minus) the Obukhov length [26]

$$L_O = \frac{\bar{T}u_*^2}{\kappa g T_*}. \quad (6)$$

For $\bar{T} = 300 \text{ K}$, $T_* = 1 \text{ K}$, $U_{\text{ref}} = 20 \text{ m/s}$ and $z_0 = 0.05 \text{ m}$, corresponding to $u_* \simeq 1.5 \text{ m/s}$, we get $L_O \simeq 170 \text{ m}$.

For $x_3 > L_O$ the mean velocity and temperature profiles become almost constant, and, in the presence of unstable stratification, turbulence consists of thermal plumes whose dynamics is determined by the convection time $\tau_{\text{conv}}(L_O)$.

We can determine the amplitude of the velocity and temperature fluctuations in the convective layer by requiring that, in stationary conditions, the turbulent heat flux is independent of the height, $u_{x_3}\tilde{T}_{x_3} \sim \text{constant}$, where u_{x_3} and \tilde{T}_{x_3} are the typical velocity and temperature fluctuations at height x_3 . From $u_{x_3} \sim x_3/\tau_{\text{conv}}(L_O)$, we then get, for $x_3 > L_O$,

$$u_{x_3} \sim \frac{u_*x_3}{L_O}, \quad \tilde{T}_{x_3} \sim \frac{T_*L_O}{x_3}. \quad (7)$$

Thermal plumes accelerate as they rise in the convective layer, and temperature gradients concurrently diminish. The rise of the thermal plumes stops at the top of the convective layer, at a typical height $x_3 = 1 \div 2 \text{ km}$, in the entrainment layer, where stratification becomes strongly stable.

A. Turbulence microstructure

Turbulent structures at scale L_O or higher are expected to generate a contribution to the noise spectrum at

frequencies much below those of interest for GW detectors. The most significant contribution is likely to come from fluctuations close to the earth's surface, and from small turbulent structures originating—through the Kolmogorov cascade—from larger eddies higher in the boundary layer. The statistical properties of turbulence can be quantified in terms of correlation functions for velocity fluctuations $C(\mathbf{x}, \mathbf{x}'; t)$ and those for temperature fluctuations $C^T(\mathbf{x}, \mathbf{x}'; t)$ appearing in Eq. (2). In HI turbulence, the spatial dependence of $C(\mathbf{x}, \mathbf{x}'; t)$ is on $\mathbf{x} - \mathbf{x}'$ only, so that we have $C(\mathbf{x}, \mathbf{x}'; t) = C^{\text{HI}}(\mathbf{x} - \mathbf{x}', t)$, $C^T(\mathbf{x}, \mathbf{x}'; t) = C^{\text{HI}, T}(\mathbf{x} - \mathbf{x}', t)$. Hence, turbulent fluctuations can be described in terms of one-time wavevector spectra $C_k^{\text{HI}} = \int d^3x C^{\text{HI}}(\mathbf{x}, 0)e^{-i\mathbf{k}\cdot\mathbf{x}}$ and $C_k^{\text{HI}, T} = \int d^3x C^{\text{HI}, T}(\mathbf{x}, 0)e^{-i\mathbf{k}\cdot\mathbf{x}}$. At sufficiently small scales, in the so-called inertial range, turbulent fluctuations obey the Kolmogorov scaling [27]

$$C_k^{\text{HI}} \sim \mathcal{E}^{2/3}k^{-11/3}, \quad (8)$$

$$C_k^{\text{HI}, T} \sim \frac{\mathcal{E}_T}{\mathcal{E}^{1/3}}k^{-11/3}. \quad (9)$$

The dimensional constants \mathcal{E} and \mathcal{E}_T in Eqs. (8) and (9) give the speed with which turbulent fluctuations at a given scale are converted to smaller-scale turbulent fluctuations. Viscous forces become dominant at sufficiently small scales, and this determines the size η_K of the smallest eddies (Kolmogorov scale):

$$\eta_K \sim \mathcal{E}^{-1/4}\nu^{3/4}, \quad (10)$$

where $\nu \simeq 0.15 \text{ cm}^2/\text{s}$ is the kinematic viscosity of air. If L is the characteristic size of the largest eddies in the flow (the so-called integral scale of vortices), and u_L and \tilde{T}_L are their characteristic velocity and temperature scales respectively,

$$\mathcal{E} \sim u_L^3/L, \quad \mathcal{E}_T \sim u_L\tilde{T}_L^2/L, \quad (11)$$

and Eqs. (8) and (9) will apply provided that $kL \gg 1$. For $u_L \sim u_* = 1.5 \text{ m/s}$ and $0.1 \text{ m} < L < L_O = 170 \text{ m}$, we would have $0.02 \text{ m}^2/\text{s}^3 < \mathcal{E} < 3.4 \text{ m}^2/\text{s}^3$, corresponding to values of the Kolmogorov length η_K below the millimeter.

To any given scale l we can associate a characteristic velocity scale $\Delta_l u \sim |\mathbf{u}(\mathbf{x} + \mathbf{l}) - \mathbf{u}(\mathbf{x})| \sim (k^3 C_k^{\text{HI}})^{-1/2}_{k \sim l^{-1}}$. From Eq. (8), then, we can define an eddy turnover time

$$\tau_k \sim \left(\frac{l}{\Delta_l u} \right)_{l=k^{-1}} \sim \mathcal{E}^{-1/3}k^{-2/3}, \quad (12)$$

which gives the typical lifetime of turbulent structures of size k^{-1} .

One may expect that at height x_3 in the PBL, turbulent microstructure at scale $k^{-1} \ll x_3$ could be considered, using HI turbulence concepts, as originating from eddies of size $L \sim x_3$ and velocity scale u_{x_3} .

Indeed, things are more complicated, at least in the surface layer, because structures with $kx_3 \gg 1$ could

be part of cascades originating from structures of size $L \sim x'_3$ at height $x'_3 > x_3$. The problem is less serious in the convective layer, where thermal plumes continuously carry smaller eddies upwards and prevent the simultaneous presence of multiple cascades at any given height. We shall deal with this issue by representing turbulence as a superposition of contributions from horizontal layers of different thickness, in which turbulence is approximated as homogeneous and isotropic.

IV. NEWTONIAN NOISE FROM HOMOGENEOUS ISOTROPIC TURBULENCE

The simplest model of NN production by atmospheric temperature fluctuations we can devise is realized by treating the PBL as an infinite layer of HI turbulence. The correlation function $C^T(\mathbf{x}, \mathbf{x}'; t)$ has a rather intricate structure in which space and time dependence are intertwined. Performing a successful analysis of $C^T(\mathbf{x}, \mathbf{x}'; t)$ heavily relies on the possibility of introducing some kind of factorization between its space and time dependence. The space dependence of the correlation function $C^T(\mathbf{x}, \mathbf{x}'; t)$ in Eq. (2) is determined by the spectrum $C_k^{\text{HI}, T}$ in Eq. (9). The time structure of $C^T(\mathbf{x}, \mathbf{x}'; t)$ is more complex. Equation (12) tells us that there is a multiplicity of decay times associated with the different spatial scales in the problem. The situation is complicated by the so-called Taylor sweep, which consists of turbulent structures being transported by both the mean wind and larger turbulent structures, while being stretched and deformed into smaller-scale turbulent structures.

The analysis of the problem is facilitated by the ordering $U > u$ which allows us, in the first approximation, to neglect the contribution of larger eddies to the transport of eddies at any given scale. A similar approach has been used in the design of some turbulent closures [28]. In this approximation, it is possible to eliminate the effect of the Taylor sweep by shifting to the reference frame of the mean wind,

$$\langle \tilde{T}(\mathbf{x}, t) \tilde{T}(0, 0) \rangle = \langle \tilde{T}(\mathbf{x} - \mathbf{U}t, t) \tilde{T}(0, 0) \rangle_U, \quad (13)$$

where $\langle \tilde{T}(\mathbf{x}, t) \tilde{T}(0, 0) \rangle_U$ can be expressed, using Eq. (9), as a superposition of Fourier modes, each decaying at the time-scale fixed by Eq. (12):

$$\langle \tilde{T}(\mathbf{x}, t) \tilde{T}(0, 0) \rangle_U = \frac{\mathcal{E}_T}{\mathcal{E}^{2/3}} \int \frac{d^3k}{(2\pi)^3} \frac{d\omega}{2\pi} k^{-11/3} h(\tau_k \omega) e^{i(\mathbf{k} \cdot \mathbf{x} - \omega t)}. \quad (14)$$

We assume the function h to be symmetric, normalized to 1, and going to zero for large values of the argument. Equation (14) tells us that, in Fourier space, the correlations for temperature fluctuations can be expressed as the product of $h(\tau_k \omega)$ times a function of k . We substitute now Eqs. (13) and (14) into Eq. (2), and obtain

after simple algebra,

$$S_g = \frac{\mathcal{E}_T}{\mathcal{E}^{2/3}} \int \frac{d^3k}{(2\pi)^3} k^{-13/3} |G_{\mathbf{k}}(r_0)|^2 \times h[\tau_k(\omega - \mathbf{k} \cdot \mathbf{U})]. \quad (15)$$

The Green function $G_{\mathbf{k}}(r_0)$ has been computed in Appendix A. For the case of HI turbulence, it reads (see Eq. (A3))

$$|G_{\mathbf{k}}(r_0)|^2 = \left(\frac{2\pi\alpha \cos\phi}{k} \right)^2 e^{-2k_{\perp} r_0}, \quad (16)$$

where, we recall, $\mathbf{k}_{\perp} \equiv (k_1, k_2, 0)$, $\cos\phi = k_1/k_{\perp}$, r_0 is the depth of the detector, and $\alpha = G\bar{\rho}/T$ is the conversion factor from temperature to acceleration fluctuations [see Eq. (1)]. In Section VI we will use Eq. (15), together with the Green function (16), as the starting point for the numerical computation of the spectral density for NN generated by HI turbulence.

We note the small- k divergence of the integrand in Eq. (15), which requires the function h to decay sufficiently fast for large values of the argument.

The fast decay of the frequency spectrum h reflects the character of the time decorrelation process as the result of the continuous stretching and scrambling of turbulent structures by the turbulent flow. This is to be opposed to the case of thermal fluctuations, where a microscopic mechanism (molecular motion) is at play, causing the correlation function $C(t)$ to be not differentiable at $t = 0$, and the associated spectrum to decay like ω^{-2} at large ω . We can verify that, with such a slow decay of frequency spectrum, the integral in Eq. (15) would be logarithmic divergent at small k .

Similar difficulties in following a Langevin-equation-based approach in turbulence have been discussed in [29], concerning subgrid modeling for large-eddy simulations of wall flows.

A. Frozen turbulence limit

An important limit of Eq. (15), which has been explored in [21], is that of frozen turbulence, in which the time-decay of correlations in the reference frame of the wind is slow and the time-decorrelation of $C^{\text{HI}, T}(\mathbf{x}; t)$ is only a consequence of the Doppler shift induced by the mean wind. The frozen turbulence limit is realized by approximating the function h in Eq. (15) with a Dirac delta, which requires the width of h , seen as a function of k , to be much smaller than both U/ω and the width of $|G_{\mathbf{k}}(r_0)|^2$. Inspection of Eqs. (15) and (16) gives us the condition

$$\tau_{\omega}/U \gg \max(r_0/U, \omega^{-1}), \quad (17)$$

which means that the structures contributing to the noise must have an eddy turnover time significantly longer than both the inverse of the frequency and the transit time

over a distance r_0 . The second condition is especially interesting: r_0/U represents the effective time the turbulent structure is effectively seen by the detector, and Eq. (17) tells us that, for a frozen turbulence hypothesis to be satisfied, the depth at which the detector is situated must not be too large. In frozen turbulence conditions, Eq. (15) takes the form

$$S_g^{ft} = \frac{\mathcal{E}_T}{\mathcal{E}^{1/3}} \int \frac{d^3k}{(2\pi)^2} k^{-11/3} |G_{\mathbf{k}}(r_0)|^2 \delta(\omega - \mathbf{k} \cdot \mathbf{U}). \quad (18)$$

Combining Eqs. (16) and (18) produces the general expression

$$S_g^{ft} = \hat{S}_g^{ft}(\psi, \omega r_0/U) \frac{\alpha^2 \mathcal{E}_T U^{8/3}}{\mathcal{E}^{1/3} \omega^{11/3}}, \quad (19)$$

where \hat{S}_g^{ft} is dimensionless, and ψ is the angle between \mathbf{U} and the detector arm (see Fig. 1). The ratio $\mathcal{E}_T/\mathcal{E}^{1/3}$ in the formula coincides with the parameter c_T^2 in [21], giving $\mathcal{E}_T/\mathcal{E}^{1/3} = 0.2 \text{ K}^2 \text{ m}^{-2/3}$.

The integral in Eq. (18) can be computed analytically. The details of the calculations are described in Appendix B, and the final result is a combination of hypergeometric functions (see Eq. (B6)).

The small frequency regime of the spectrum can be directly inferred from Eq. (19). As discussed in Appendix C, \hat{S}_g^{ft} has as a finite limit $S_g^{ft}(\psi, 0) = S_g^{ft}(\psi)$, which implies a power-law scaling in ω for the dimensional spectrum S_g^{ft} (this can also be verified by taking the limit of the exact expression (B6)).

The regime $\omega r_0/U \gg 1$ is analyzed in Appendix C and gives us the exponential behavior

$$S_g^{ft} \sim \frac{\mathcal{E}_T \alpha^2 U^{8/3} \cos^2 \psi}{\mathcal{E}^{1/3} \omega^{11/3}} \left(\frac{U}{\omega r_0} \right)^{\frac{1}{2}} \exp \left(-\frac{2\omega r_0}{U} \right). \quad (20)$$

It is quite interesting to compare our Eq. (20) with the results of Ref. [21], where also the NN generated by HI turbulence in the frozen limit has been analyzed. We see that the exponential behavior of the noise spectrum as a function of ω and r_0 found in Ref. [21] holds only for frequencies ω much higher than U/r_0 .

B. Weak wind regime

The weak wind regime is realized for $\omega \tau_\omega/U \ll 1$, which corresponds to approximating $h[\tau_k(\omega - \mathbf{k} \cdot \mathbf{U})] \simeq h(\omega \tau_k)$ in Eq. (15). The analysis in Appendix C produces, in this case, the power-law behaviors

$$S_g^{ww} \sim \frac{\mathcal{E}_T \alpha^2}{\mathcal{E}^{2/3}} \times \begin{cases} k_\omega^{-16/3} r_0^{-2}, & k_\omega r_0 \gg 1, \\ k_\omega^{-10/3}, & k_\omega r_0 \ll 1, \end{cases} \quad (21)$$

where

$$k_\omega = \mathcal{E}^{-1/2} \omega^{3/2} \quad (22)$$

is the inverse size of vortices with eddy turnover time ω^{-1} .

V. NEWTONIAN NOISE FROM TURBULENCE IN THE PBL

In this section, we go beyond the isotropic and homogeneous approximation for turbulence by building a more realistic model, in which the vertical structure of the PBL is fully taken into account. Conversely, we continue to assume homogeneous correlations horizontally. Following an approach described in [30], we model turbulence in the PBL as a superposition of HI turbulence contributions in horizontal layers $[0, \bar{x}_3]$, where \bar{x}_3 ranges from a minimum height $x_{3,\min} \sim z_0$ —marking the transition to the region where turbulence is strongly affected by the roughness geometry—to a maximum height L_{PBL} identifying the top of the PBL. As a rule of thumb, one usually sets $x_{3,\min} = 10z_0$ [24]. The latter choice, however, could cut potentially important contributions from vortices at the lower end of the logarithmic region. In our model, therefore, we choose a value in-between, $x_{3,\min} = ez_0$,¹ to identify the smallest integral-scale temperature fluctuations contributing to the noise. These temperature fluctuations have amplitude T_* and eddy turnover time $\tau_{x_{3,\min}}^{-1} \sim x_{3,\min}/u_*$. Thus, a smaller $x_{3,\min}$ will correspond to a stronger high-frequency contribution to the noise. Indeed, we will show in Section VI that the specific choice of $x_{3,\min}$ in terms of z_0 only alters the high-frequency portion of the spectral density, which is however always below the sensitivity curve of ET for reasonable values of the parameters (see bottom panel of Fig. 8).

The contributions to the temperature fluctuation $\tilde{T}(\mathbf{x}, t)$ from layers with $\bar{x}_3 \geq x_3$, $\tilde{T}(\mathbf{x}, t|\bar{x}_3)$, are assumed uncorrelated. The spectrum in each layer can be assumed to obey Kolmogorov scaling only for $k\bar{x}_3 \gg 1$. We must thus extend Eqs. (9) and (12) to integral scales $k\bar{x}_3 \leq 1$. The simplest possibility is to assume a sharp transition into the Kolmogorov scaling regime exactly at $k\bar{x}_3 = 1$, i.e. to set

$$C_k^{\text{HI,T}}(\bar{x}_3) \sim \frac{\tilde{T}_{\bar{x}_3} \bar{x}_3^3}{\max(1, (k\bar{x}_3)^{11/3})}; \quad (23)$$

$$\tau_k(\bar{x}_3) \sim \frac{\bar{x}_3}{u_{\bar{x}_3} \max(1, (k\bar{x}_3)^{2/3})}, \quad (24)$$

where Eq. (11) has been used.

For simplicity, the effect of the Taylor sweep in each layer is approximated with that of a constant wind $U_{\bar{x}_3}$. The temperature correlation resulting from the superposition of the contributions in Eqs. (23) is in the form

$$C_{\mathbf{k}_\perp, \omega}^T(x_3, x'_3) = \int_{\max(x_3, x'_3)}^{L_{PBL}} \frac{d\bar{x}_3}{\bar{x}_3} \int \frac{d^3k}{2\pi} C_k^{\text{HI,T}}(\bar{x}_3) \times h[\tau_k(\bar{x}_3)(\omega - \mathbf{k} \cdot \mathbf{U}_{\bar{x}_3})] e^{ik_3 \cdot (x_3 - x'_3)}. \quad (25)$$

¹ The choice is arbitrary, but it allows a smooth transition, in the vertical wind speed profile, from a linear behavior in the roughness layer, $U_{x_3} \propto x_3/x_{3,\min}$, to the logarithmic profile above $U_{x_3} \propto \ln(ex_3/x_{3,\min})$.

As in the case of Eq. (15), the spectrum h is evaluated at the Doppler-shifted frequency $\omega - \mathbf{k} \cdot \mathbf{U}_{\bar{x}_3}$, generated by expressing correlations in the reference frame of the wind in the layer \bar{x}_3 . Note the factor \bar{x}_3^{-1} in the integral, which guarantees that all layers have equal weight.

We substitute Eq. (25) together with Eqs. (23) and (24) and the propagator (A5) calculated in Appendix A into Eq. (2) and obtain, after straightforward algebra,

$$S_g = \frac{\alpha^2}{\pi} \int_{x_{3,\min}}^{L_{PBL}} d\bar{x}_3 \int_0^{+\infty} dk \int_0^1 dp \frac{p}{\sqrt{1-p^2}} \times \frac{\bar{x}_3^3 \tilde{T}_{\bar{x}_3}^2 A(\mathbf{k}, \bar{x}_3) B(\mathbf{k}, \bar{x}_3) e^{-2kpr_0}}{U_{\bar{x}_3} \max[1, (k\bar{x}_3)^{13/3}]}, \quad (26)$$

where $p = k_{\perp}/k$, and

$$A = \int_0^{2\pi} d\phi \cos^2 \phi h[\tau_k(\bar{x}_3)(\omega - \mathbf{k} \cdot \mathbf{U}_{\bar{x}_3})], \quad (27)$$

$$B = k^2 \int_0^{\bar{x}_3} dx_3 dx'_3 e^{ik_3(x_3 - x'_3) - k_{\perp}(x_3 + x'_3)} = 1 + e^{-2k_{\perp}x_3} - 2e^{-k_{\perp}x_3} \cos(k_3\bar{x}_3). \quad (28)$$

In Section VI we will use Eq. (26) as a starting point for the numerical computation of the spectral density for NN generated by turbulence in the PBL. We note the scaling $\tilde{T}_{\bar{x}_3}^2/U_{\bar{x}_3} \propto \bar{x}_3^{-3}$ for $\bar{x}_3 > L_O$ in Eq. (26), which descends from Eq. (7). This suggests that the dominant contribution to S_g comes from the surface layer, where $\tilde{T}_{\bar{x}_3}^2/U_{\bar{x}_3} = T_*^2/u_*$. Numerical analysis confirms this indication. This prompts us to replace $L_{PBL} \rightarrow L_O$ in Eq. (26), thus approximating the noise production in the PBL with the contribution in the surface layer.

To analyze the contribution to the noise in the surface layer, it is convenient to shift to the so-called wall units [24], which we identify with a hat:

$$\hat{\omega} = \frac{\omega z_0}{u_*}, \quad \hat{r}_0 = \frac{r_0}{z_0}, \quad \hat{L}_O = \frac{L_O}{z_0}. \quad (29)$$

Note from Table I, that for reasonable values of r_0 and z_0 , we have always $\hat{r}_0 \gg 1$. In terms of wall units, Eq. (26) can be written in the form

$$S_g = \frac{\alpha^2 T_*^2 z_0^3}{u_*} \hat{S}_g(\hat{\omega}, \hat{r}_0, \hat{L}_O), \quad (30)$$

with \hat{S}_g dimensionless.

A. Limit behaviors

The asymptotic analysis in Appendix E tells us that, in the two limits of small and large $\hat{\omega}$, the dominant contribution to \hat{S}_g comes from turbulent structures in the integral range ($k\bar{x}_3 < 1$) and in the inertial range ($k\bar{x}_3 > 1$), respectively. This is associated with the observation that the large ω contribution to S_g is increasingly concentrated at smaller \bar{x}_3 .

The mechanism for the separation between small and large frequency behavior can be understood by considering that the frequency ω selects, as dominant contributors to S_g , turbulent structures with size k_{ω}^{-1} , such that either the eddy turnover time τ_k or the transit time $(kU_{\bar{x}_3})^{-1}$ is $\sim \omega^{-1}$. A maximum frequency for the production of integral range vortices of size k_{ω}^{-1} is then identified by $k_{\omega}z_0 \sim 1$, as smaller integral-scale vortices would have to reside inside the roughness of the terrain.

The different scaling of the contributions to S_g from integral and inertial range turbulent structures is associated with a transition from a small to a large frequency behavior that is characterized by an increase in the decay rate with frequency. Indeed, the asymptotic analysis in Appendix E gives us, for ω^{-1} shorter than the eddy turnover time of integral scale vortices at height z_0 ,

$$\hat{S}_g \sim \hat{\omega}^{-8} \hat{r}_0^{-2}, \quad \min(\hat{\omega}, \hat{r}_0) \gg 1, \quad (31)$$

which is Eq. (E5). This equation tells us that we will always have a $1/r_0^2$ behavior of S_g at large frequencies and for large values of r_0 .

For small $\hat{\omega}$, instead, we have two possible behaviors depending on the magnitude of \hat{r}_0 (see Eq. (E7)):

$$\hat{S}_g \sim \begin{cases} \hat{x}_{3,\max}^3, & 1 \gg \hat{\omega} \hat{r}_0 \\ \hat{r}_0^{-2} \hat{x}_{3,\max}^5, & \hat{\omega} \hat{r}_0 \gg 1 \gg \hat{\omega}, \end{cases} \quad (32)$$

where

$$\hat{x}_{3,\max} = \min(\hat{\omega}^{-1}, \hat{L}_O), \quad (33)$$

and where the ratio r_0/u_* in $\hat{\omega} \hat{r}_0 = \omega r_0/u_*$ is the eddy turnover time of integral scale vortices at height r_0 . Thus, at small frequencies, power-law decay in r_0 of the noise spectrum will ensue for $r_0 \sim u_*/\omega$, which is the size (and the height) of integral scale vortices with eddy turnover time ω^{-1} . As already remarked, for reasonable values of r_0 and z_0 , we always have $\hat{r}_0 \gg 1$, which is why we have chosen to disregard the range $\hat{\omega} \gg 1 \gg \hat{r}_0$ in Eq. (31) in the first place. Notice, moreover, that the $1/r_0^2$ behavior arises also in the weak-wind regime of the HI approximation (see Eq. (21)). As we show in Appendix F, this is a general behavior arising whenever the effect of eddy decay dominates over wind advection and r_0 is large.

VI. RESULTS

In this section we numerically compute and analyze the behavior of the power spectra obtained from Eq. (2) for the three different cases discussed in this paper: (a) HI turbulence in the frozen limit, (b) HI turbulence with finite correlation time, and (c) turbulence in a horizontally homogeneous PBL. Specifically, for case (a), we use the expression (18), while for cases (b) and (c), as starting point for the numerical computation of the power spectra, we use the more general Eqs. (15) and (26), respectively. The extended set of data presented and related to

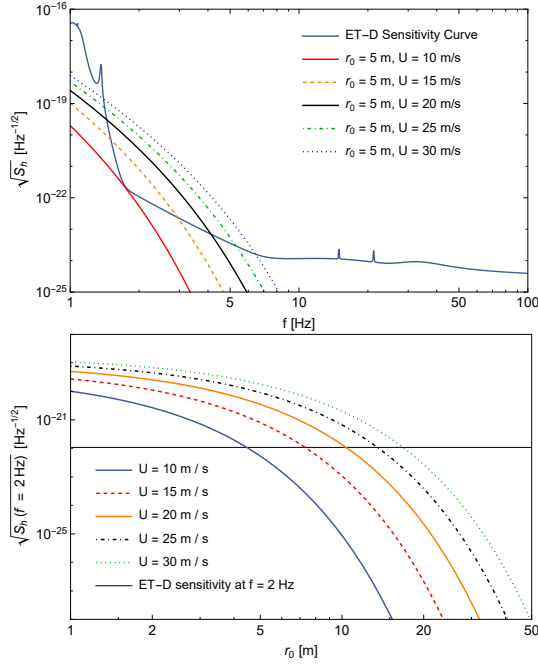


Figure 3. HI turbulence - frozen limit. **Top panel:** noise spectra as functions of the frequency $f = \omega/(2\pi)$ at fixed detector depth r_0 and with varying wind speed U . **Bottom panel:** strain spectrum for $f = 2 \text{ Hz}$ as a function of the detector depth r_0 for selected values of the wind speed U . In all cases we have taken $\psi = 0$.

this work are available online [31]. Moreover, we compare the resulting spectra with the ET-D sensitivity curve, to investigate the possible impact of atmospheric NN on next-generation GW detector measurements. Note that the ET-D sensitivity curve is expressed in terms of the strain power spectrum S_h , which is related to the acceleration power spectrum S_g in Eq. (2) by the relation

$$S_h = 4 \frac{S_g}{\omega^4 L_{\text{arm}}^2}, \quad (34)$$

where L_{arm} is the length of the detector arm, while the factor of 4 takes into account the number of test-masses in the detector. Indeed, one can assume that the NN contributions on each test mass are uncorrelated, since those arising from correlated signals between two or more test masses are expected to be negligible [18, 21]. We rescale the modeled spectra according to Eq. (34).

(a) HI turbulence: frozen limit—In the frozen limit, the frequency spectrum of the temperature fluctuations (function h in Eq. (15)), is simply a Dirac delta (see Eq. (18)). This allows us to use the analytic expression for the integral (18) in terms of a sum of hypergeometric functions provided in Eq. (B6). The noise curves obtained in this limit, for fixed r_0 and varying U , are shown in the upper panel of Fig. 3 and compared with the sensitivity curve of ET-D. We also show the variation of the

strain spectrum at the fixed pivotal value of the frequency of 2 Hz, as a function of the depth r_0 (bottom panel of Fig. 3). For all the curves in Fig. 3, we have set the coefficient $c_T^2 = \mathcal{E}_T/\mathcal{E}^{1/3}$ in Eq. (18) equal to its value in [21], $c_T^2 = 0.2 \text{ K}^2 \text{ m}^{-2/3}$. Here, and in the following cases (HI turbulence with finite correlation time, and inhomogeneous turbulence), we have set $\psi = 0$, which corresponds to wind blowing parallel to the detector arm (see subsection (c) for a discussion of the dependence of the spectra on ψ).

As already discussed below Eq. (20), the NN is exponentially suppressed for both large frequencies and large detector depths. In particular, it is worth noting that the noise curve is below the ET sensitivity curve for $r_0 \gtrsim 30 \text{ m}$ and for frequencies $f \gtrsim 5 \text{ Hz}$, where $f = \omega/(2\pi)$. Moreover, the larger the wind speed, the larger the noise amplitude, as explicitly shown in Fig. 3. The bottom panel of Fig. 3 also shows that, for $f = 2 \text{ Hz}$, if $r_0 \lesssim 5 \text{ m}$ and $U \geq 10 \text{ m/s}$, the NN spectrum is comparable or above the sensitivity of ET-D. The same happens if $r_0 \lesssim 20 \text{ m}$ and $U \simeq 30 \text{ m/s}$. The frequency range considered in the plot is not wide enough to visualize the power-law behavior predicted by Eq. (B6) in the $\omega \ll U/r_0$ limit. We have verified that the latter arises at very small frequencies $f \ll 1 \text{ Hz}$, for the values of U and r_0 considered here. Alternatively, very large values U or very small values of r_0 would be required. If the interferometer is built underground, however, r_0 is at least $\sim 1 \text{ m}$; on the other hand, winds stronger than 30 m/s are very unlikely.

(b) HI turbulence: finite correlation time—To go beyond the frozen turbulence approximation, an explicit form of the function h in Eq. (15) must be selected. However, such a choice is not straightforward. In fact, the functional dependence of h on the physical parameters relies on the underlying dynamics of the turbulent structures, whose detailed knowledge is still missing. A reasonable and likewise simple form for the temporal correlation spectrum in Eq. (15), which satisfies the conditions given in Section IV, is a Gaussian function

$$h[\tau_k(\omega - \mathbf{k} \cdot \mathbf{U})] = e^{-\tau_k^2(\omega - k_{\perp} U \cos(\phi - \psi))^2}. \quad (35)$$

We have verified that other choices of h , such as that of a top-hat function, do not produce significantly different results. Using Eq. (35), the integral (15) has no closed-form solution, thus the noise spectra must be computed via numerical integration.

The integrand in Eq. (15) as well as in Eq. (26) is concentrated in a tiny section of the integration domain, whose shape is highly dependent on the parameters involved. This makes numerical integration by quadratures cumbersome. The integrals have thus been computed using the VEGAS algorithm [32], which exploits a Monte Carlo technique with importance sampling and is ideally suited for multidimensional integrals. It should be pointed out that, with this approach, the numerical

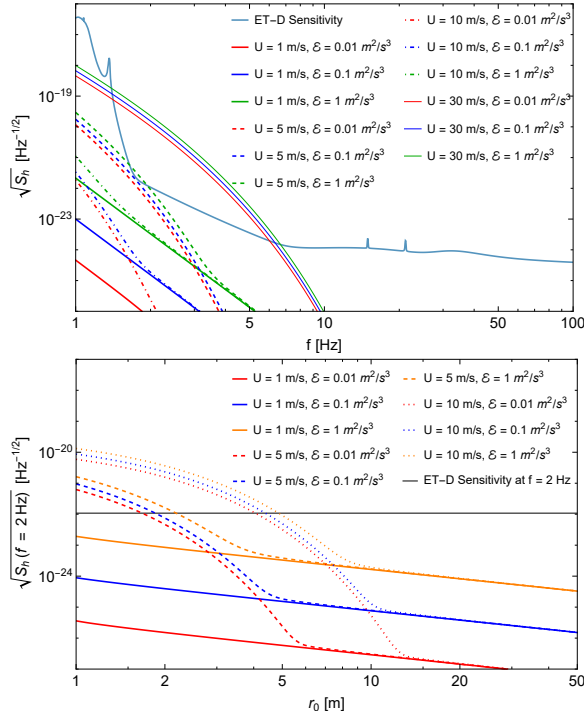


Figure 4. HI turbulence - finite correlation time. **Top panel:** noise spectra as a function of the frequency f for $r_0 = 5 \text{ m}$ and $\psi = 0$ and for selected values of the parameters in the HI approximation with Gaussian time correlations. **Bottom panel:** noise spectra as a function of the detector depth r_0 for $f = 2 \text{ Hz}$ and $\psi = 0$ and for selected values of the parameters in the HI approximation with Gaussian time correlations.

estimation is highly computational consuming (~ 3 core-hour for a single value of S_h). Therefore, the integrals have been computed by using the HYDRA framework [33], which is designed to perform data analysis and numerical integration tasks on massively parallel platforms, commonly used in the high-energy, particle physics community. Using this tool, we carried out the integrals in Eqs. (15) and (26) obtaining our results with a sub-percent precision in a reasonable amount of time.

We have repeated the analysis in Fig. 3, for different values of U and r_0 , and of the new parameter \mathcal{E} , which sets the scale of the eddy turnover time τ_k (see Eq. (12)). We have considered values of \mathcal{E} in the range $0.01 \text{ m}^2/\text{s}^3 \lesssim \mathcal{E} \lesssim 1 \text{ m}^2/\text{s}^3$ (see discussion following Eq. (11)). For consistency with the frozen turbulence case, we have taken $\mathcal{E}_T = c_T^2 \mathcal{E}^{1/3}$, with $c_T^2 = 0.2 \text{ K}^2 \text{ m}^{-2/3}$. As in the previous subsection, we limited our analysis to the case $\psi = 0$.

The results are shown in Fig. 4. The curves are quite similar to those in Fig. 3. In general, the noise still decays for large detector depths and large frequencies, while it increases with the wind speed and with \mathcal{E} . The latter reflects the increase in the amplitude of the temperature fluctuations with $\mathcal{E}_T = c_T^2 \mathcal{E}^{1/3}$, which implies, through Eq. (12), an increase of the characteristic frequency of the fluctuations as well. However, a new feature, not present

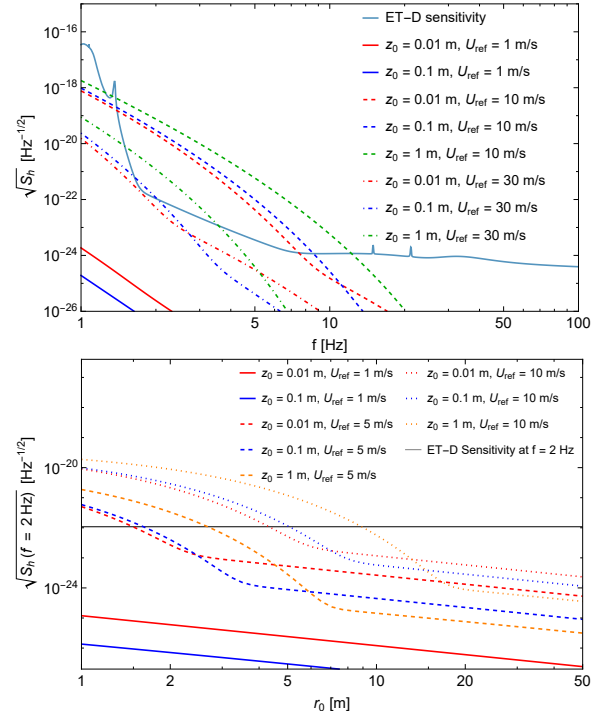


Figure 5. Inhomogeneous turbulence. **Top panel:** noise spectra as a function of the frequency f for $r_0 = 5 \text{ m}$ and $\psi = 0$ and for selected values of the parameters in the surface-layer model with Gaussian time correlations. **Bottom panel:** noise spectra as a function of the detector depth r_0 for $f = 2 \text{ Hz}$ and $\psi = 0$ and for selected values of the parameters in the surface-layer model with Gaussian time correlations.

in the frozen regime, is observed in both panels, namely a transition to a power-law regime in f and r_0 if f is very large, U is very small or r_0 very large (see Eq. (21)). At intermediate values of the parameters (take, for instance, the curve with $U = 5 \text{ m/s}$, $\mathcal{E} = 0.1 \text{ m}^2/\text{s}^3$ in the top panel of Fig. 4), the noise curves show a transition from exponential (at low frequencies) to power-law (at large frequencies) behavior. As expected, the noise curves show a weak dependence on \mathcal{E} as long as the dominant contribution to the noise comes from wind transport rather than from vortex decay. This occurs for $U \gtrsim 10 \text{ m/s}$. This feature makes the noise curves for HI turbulence with Gaussian time correlation and those obtained in the frozen approximation comparable in the parameter region of interest, i.e. that in which the noise curves are close to the ET-D sensitivity curve. Indeed, it can be seen that, in this exponentially-damped regime, the NN from turbulence with finite correlation time and frozen turbulence have roughly the same impact on the GW detector. On the contrary, the frequency at which the transition between the two regimes (exponential damping and power-law scaling) occurs, strongly depends on the value of \mathcal{E} . In particular, we see that the power-law behavior shifts to larger frequencies for smaller \mathcal{E} .

Inspection of Fig. 4 also shows that going beyond

the frozen approximation changes only slightly the impact of both the wind speed U and the depth r_0 on power spectrum noise curves at small frequencies. The differences between the noise curves for HI turbulence with Gaussian time correlation and those for frozen turbulence are quite small. At a fixed wind speed of 10 m/s, for instance, both curves cut the ET-D sensitivity curve at $r_0 \approx 4 - 5$ m.

(c) Inhomogeneous turbulence—The noise spectrum is now described by Eq. (26). We have proceeded as in the (b) case, and assumed Gaussian time correlations, as described in Eq. (35). The noise spectrum has been evaluated from Eq. (26), as a function of the experimentally accessible quantities U_{ref} , z_0 and T_* . The quantity T_* , which gives the scale of the temperature fluctuations, enters the expression for S_g (26) as a scale factor and has been fixed at the reference value $T_* = 1$ K. For z_0 we have taken values corresponding to situations ranging from that of bare soil to that of a forest or a city district, as described in Table I. As in the previous HI turbulence cases, we have set $\psi = 0$.

The noise amplitude increases with the wind speed U_{ref} and, for small frequencies, with the roughness length z_0 . This is not surprising, considering that the turbulence intensity, parameterized by u_* , is proportional to U_{ref} and it increases with z_0 through Eq. (4). In the high-frequency region, instead, in correspondence with the onset of the power-law behavior, the noise curves are characterized by $\sqrt{S_h}$ scaling as $z_0^{-3/2}$, as predicted by Eqs. (30) and (31). We also recall that a significant contribution to high frequencies fluctuations is produced in the region near the ground, where the parameter $x_{3,\text{min}} \sim z_0$ plays the role of a cutoff (see Eq. (26)); we will return to this point at the end of the section. We note that, since T_* is the same in all curves, the increase in the noise amplitude with U_{ref} and z_0 is a consequence of the increase of the characteristic frequency of the fluctuations only.

The curves in the top panel of Fig. 5, like those in the top panel of Fig. 4, are characterized by a transition from an exponential to a power-law behavior at sufficiently small values of U_{ref} and z_0 . A transition to a power-law, this time for r_0 , is observed also in the bottom panel of Fig. 5, analogous to the one observed in Fig. 4. The crossover point in r_0 shifts to the right for large values of U_{ref} and z_0 , which is consistent with the predictions in the asymptotic large ω and small ω limits provided by Eqs. (31) and (32). This is not surprising, since U_{ref} plays in the inhomogeneous model the same role played by U in the HI model. For very small frequencies, moreover, the spectra are characterized by another power-law scaling, which however can be observed only for $f \lesssim 2$ Hz and for large values of U_{ref} .

Another interesting feature is the scaling with the parameter z_0 , describing the roughness of the terrain. Indeed, the spectra scale as $\sim z_0^{-3}$ for $\omega \gg u_*/z_0$ while, for $\omega \ll u_*/z_0$, they first increase with z_0 and then they be-

come almost independent of this quantity (see Eqs. (31) and (32)). Similarly to what happens with the parameter \mathcal{E} in the HI case, the weak dependence of the noise curves on the parameter z_0 is a characteristic of the regime where wind transport dominates over vortex-decay. Again, this is a nice feature, allowing for easy comparison of the curves for inhomogeneous and homogeneous turbulence in the regions where they are close to the ET-D sensitivity curve.

The last interesting point is the dependence of the spectra on ψ . Indeed, in some regimes (see, e.g., Eq. (20)), the spectra could depend strongly on this parameter. Anyway, we expect S_h to be the maximum for $\psi = 0$. Indeed, in Fig. 7, we show that, for reasonable values of the parameters, S_h varies at most by a factor ~ 2 .

On a semi-quantitative level, the results of the inhomogeneous model confirm those obtained in the HI one (both in the general case and in the frozen approximation limit). Indeed, for fixed values of the parameters (either U or r_0), the noise spectra in the three cases have comparable orders of magnitude, at least in the regions close to the sensitivity curve of ET-D. When the detector is located near the earth's surface, the power spectrum curves cut the ET-D sensitivity and are well above it in the frequency region 2 – 10 Hz. On the other hand, in the frequency band considered here, the noise curves go below the sensitivity curve only when the detector is located at least 50 m underground (see top panel of Fig. 6). We see, however, that for large values of U_{ref} , i.e. $U_{\text{ref}} \sim 30$ m/s, the noise curve is only a factor ~ 5 below the ET-D sensitivity curve, which is a worryingly close range, considering the fact that our models are providing only order of magnitude estimates. The situation is confirmed if we go to greater depths. Consistently with the general scaling r_0^{-1} of $\sqrt{S_h}$ derived in Appendix F, the noise spectra are only a factor of $\sim 10 - 20$ below the sensitivity curve, for $r_0 \sim 100 - 200$ m, respectively, (see bottom panel of Fig. 6).

Wavevector cutoffs and finite-size effects—For all the calculations in the present section, we have adopted a maximum wavevector k_{max} equal to the inverse of the Kolmogorov scale η_K^{-1} defined in Eq. (10), and we have set the parameter $x_{3,\text{min}} = ez_0$ as the lower bound of integration in Eq. (26). In the inhomogeneous turbulence case of Eq. (26), we have carried out the integral over \bar{x}_3 up to a reference height $L_{\text{FBL}} = 2$ km, but the contribution at $\bar{x}_3 > L_0$ turned out to be negligible.

The dependence of S_h on the parameters k_{max} and $x_{3,\text{min}}$ is rather different. In the top panel of Fig. 8, we show the effect of lowering the cutoff k_{max} on the noise spectrum. We limit our analysis to the inhomogeneous turbulence case, setting, as usual, $r_0 = 5$ m as a reference depth at which the noise is expected to be above the sensitivity threshold for the ET detector. We see that, when k_{max}^{-1} approaches the meter range, the high-

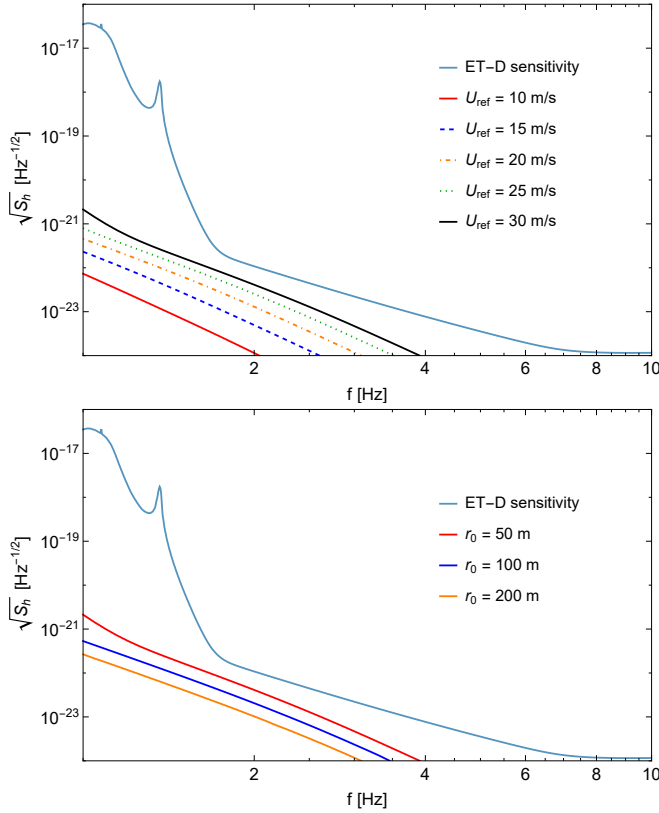


Figure 6. **Top panel:** Noise spectra for the inhomogeneous model as a function of the frequency f for $r_0 = 50$ m and for selected values of U_{ref} . **Bottom panel:** Noise spectra for the inhomogeneous model as functions of the frequency for selected values of r_0 and $U_{\text{ref}} = 30$ m/s. We fixed the values of the other parameters to: $z_0 = 0.1$ m and $\psi = 0$.

frequency portion of the noise spectrum is increasingly damped. Inspection of the top panel of Fig. 8 indicates that noise-damping occurs above the kink, signaling the transition from an exponential behavior dominated by wind transport to a power-law behavior dominated by eddy decay. However, for sufficiently small k_{max} , i.e. $2\pi k_{\text{max}}^{-1} \sim 1 - 2$ m, this transition does not occur in the frequency-band considered here, and only exponentially-damped “frozen-like” contributions are present. This is because vortices of this size have a very long decay time (see Eq. (12)) compared to the advection time of the wind.

A similar situation occurs, as illustrated in the bottom panel of Fig. 8, varying $x_{3,\text{min}}$. In this case, the high-frequency portion of the noise spectrum is increasingly damped as $x_{3,\text{min}}$ gets larger. The result is consistent with the observation in Section V A that the contribution to the high-frequency portion of the NN spectrum is produced primarily by temperature fluctuations near the ground.

The present analysis tells us that numerical simulation of the atmospheric flow, say, by large-eddy simulation

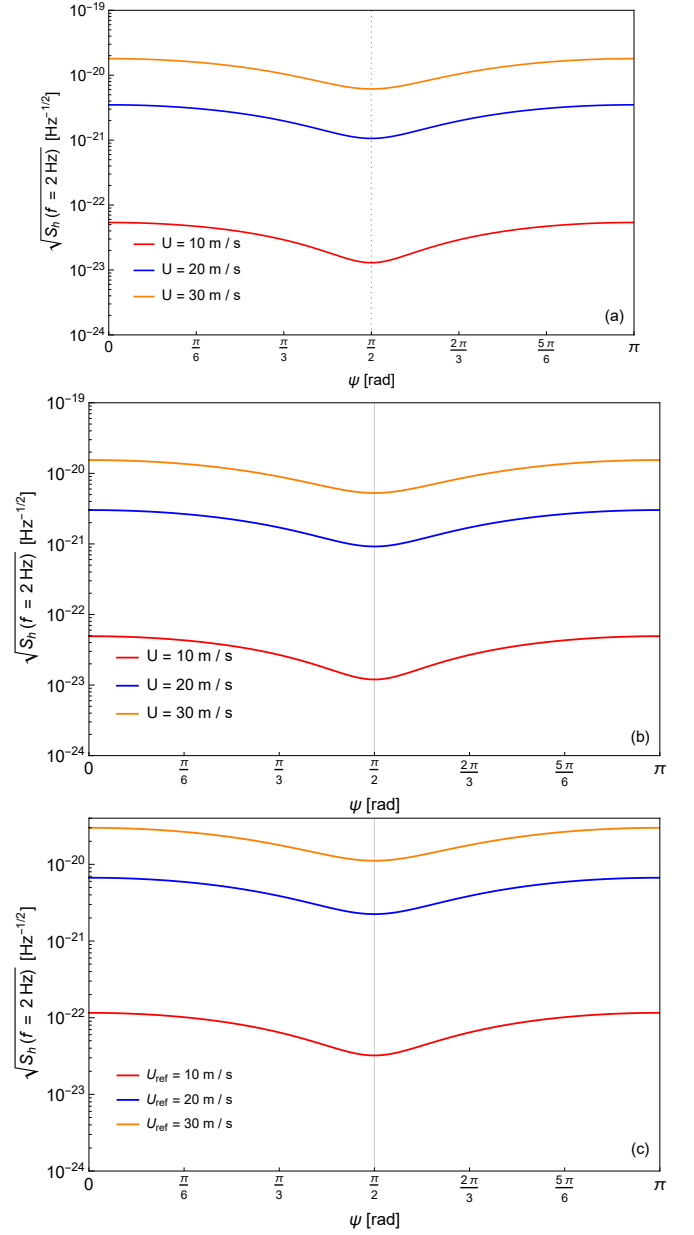


Figure 7. Noise spectra as a function of ψ in the three cases of HI turbulence - frozen case (a); HI turbulence - finite correlation time (b) and inhomogeneous turbulence (c), at varying U (upper two panels) and U_{ref} (lowest panel). We fixed the values of the other parameters to: $f = 2$ Hz, $r_0 = 5$ m, $\mathcal{E} = 0.1 \text{ m}^2/\text{s}^3$, $z_0 = 0.1$ m.

[34], would allow direct evaluation of the NN only for frequencies below a maximum that is an increasing function of k_{max} and $x_{3,\text{min}}^{-1}$. Frequencies above this maximum would require some kind of parameterization.

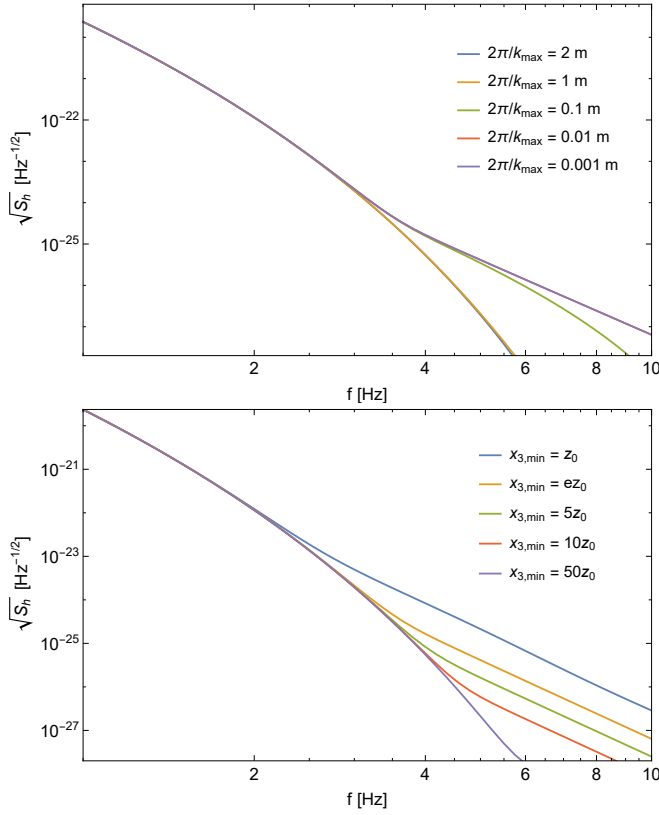


Figure 8. Inhomogeneous turbulence. **Top panel:** dependence of the noise spectrum on the wavevector cutoff k_{\max} . **Bottom panel:** dependence on the minimum height $x_{3,\min}$ of the vortices contributing to the noise. Values of the parameters in the two cases: $r_0 = 5$ m, $z_0 = 0.1$ m, $U_{\text{ref}} = 10$ m/s and $\psi = 0$.

VII. CONCLUSIONS

In this paper, we have built models for the NN generated by atmospheric turbulence, which represent a reliable tool for the assessment of the impact of atmospheric noise on third-generation GW detectors. This has been done by improving previous models for temperature-fluctuation induced atmospheric NN. Owing to their basic assumptions (frozen in time, HI turbulence) the latter are not reliable enough in the frequency bandwidth and for the sensitivity levels of third generation GW detectors. This improvement has been made possible by building both models for HI turbulence with finite correlation time for temperature fluctuations and models which also take into account the strong inhomogeneity of turbulence along the vertical direction.

We have also computed the spectral density of the NN for the three classes of models as a function of the characteristic physical parameters, and compared it with the sensitivity curve of the ET detector in the xylophone configuration. The NN signal shows two kinds of regimes, one in which it behaves exponentially and the other in which it shows a power-law behavior. The first appears to

be the signature of the dominance of wind transport and the exponential dependence on the depth of the detector, of the Green function connecting temperature fluctuations and NN. Since in a wind-dominated regime, this dependence is weighed by a characteristic scale which is the ratio of the wind velocity and the frequency, the result is an exponential scaling of the NN with both the depth of the detector and the frequency. Whenever we depart from this regime (either because eddy decay becomes an important factor, or because the depth of the detector is large), the NN dependence on the wind velocity, frequency and detector depth is a power law. While the power spectra scale with the velocity and the frequency with a power-law which is model dependent, the exponent characterizing the r_0 scaling is fixed at -2 by the properties of the gravitational propagator. Departures from exponential behavior occur for high frequencies, or very small frequencies, the latter being out of the regime of interest for ET anyway. Moreover, in the regions of interest for ET, the NN power spectra show a very weak dependence on the parameters of the models, apart from the wind speed U and the depth r_0 . Taken together, these two facts explain why the models of HI frozen turbulence used to date worked well in the assessment of the impact of atmospheric NN for second-generation GW detectors [18, 21].

We have then compared the NN power spectrum calculated with our models with the sensitivity curve of ET. We have found that the atmospheric NN contribution is above the sensitivity curve in the low-frequency band when the detector is placed on the surface and/or when the wind speed is relatively large. Thus, our main result is that NN generated by atmospheric turbulence represents an important source of noise for third-generation GW detectors, which therefore must be taken into consideration and accurately analyzed, e.g. using numerical simulations. This is of paramount importance, especially if the detector has to be built on the earth's surface.

On the other hand, we have also found that passive mitigation of atmospheric NN is only partially effective. Although placing the detector underground suppresses the atmospheric NN contribution, the rather weak, $1/r_0$, decay of the noise signal implies that even an underground construction at great depth may not be enough to suppress the noise completely. Even at $r_0 \sim 200$ m, the noise amplitude curve, despite being always below the sensitivity curve of ET, remains close to it in the low-frequency region. On the other hand, our modeling of turbulence provides only order of magnitude predictions. An inaccuracy of an order of magnitude in our estimates of the power spectrum should therefore be taken into account. Considering this fact and the proximity of the noise amplitude to the sensitivity of the detector, at least in strong wind situations (~ 30 m/s) (see Fig. 6), numerical simulations of the atmospheric flow (taking into account the orography in the detector region) and on-site measurements are advisable.

In this regard, we expect our results to be relevant

for any evaluation of NN by numerical simulation of the atmospheric flow, as atmospheric codes (such as, e.g., large-eddy simulations [34]) have a grid scale that is typically above that of fluctuations contributing to the NN.

ACKNOWLEDGEMENTS

We thank the Newtonian noise research group of the SARGRAV project and in particular Jan Harms, for helpful discussions and comments.

Appendix A: Green function evaluation

To compute the Fourier transform of the gravitational propagator, we consider the detector at depth r_0 below the earth's surface, which will be considered as a flat infinite plane. We first choose a Cartesian system of coordinates x_1, x_2 and x_3 , with origin at the test mass of the detector, and with x_1 laying along the detector arm, while x_3 will be along the vertical.

Computations can be more easily performed by adopting the cylindrical system of coordinates $\mathbf{x} = (x_\perp, \varphi, x_3)$, where φ is the azimuthal angle, while $x_\perp = (x_1^2 + x_2^2)^{1/2}$ refers to the direction perpendicular to x_3 (see Fig. 1). Moreover, we will make use of the following expressions

$$G(\mathbf{x}; r_0) = -\alpha \partial_{x_1} H(\mathbf{x}; r_0); \quad (\text{A1a})$$

$$H(\mathbf{x}; r_0) = \frac{\theta(x_3 - r_0)}{(x_\perp^2 + x_3^2)^{1/2}}. \quad (\text{A1b})$$

The Fourier transform of Eq. (A1b) then reads

$$H_{\mathbf{k}}(r_0) = \int_{r_0}^{\infty} dx_3 \int_0^{+\infty} dx_\perp x_\perp \int_0^{2\pi} d\varphi \times \frac{\exp[-i(k_3 x_3 + k_\perp x_\perp \cos \varphi)]}{(x_\perp^2 + x_3^2)^{1/2}} \quad (\text{A2})$$

where $\mathbf{k} = (\mathbf{k}_\perp, k_3)$ and $\mathbf{k}_\perp \equiv (k_1, k_2)$.

When dealing with HI turbulence, correlations have to be computed in the whole three-dimensional Fourier space. Equations (A1a) and (A2) together yield

$$G_{\mathbf{k}}(r_0) = -\frac{2\pi\alpha \cos \phi}{k_\perp + ik_3} e^{-(k_\perp + ik_3)r_0}. \quad (\text{A3})$$

where we have defined $\cos \phi = k_1/k_\perp$.

In more realistic cases, things have to be treated more carefully, as we might have inhomogeneities along one or more axes. In inhomogeneous turbulence, for instance, we have inhomogeneities along the x_3 -axis due to the inhomogeneous wind profile. Since correlations on the plane orthogonal to x_3 are assumed to be homogeneous in our model (see Section V), the Green function will be simply given by the x_\perp and φ integrals in Eq. (A2), which yield

$$G_{\mathbf{k}_\perp}(x_3, r_0) = -2\pi i \alpha \theta(x_3 - r_0) \cos \phi e^{-k_\perp x_3} \quad (\text{A4})$$

Finally, since the effects of turbulence along the vertical will be integrated from the earth's surface up to infinity, we simply have to translate the origin of the system of coordinates along the x_3 -axis by r_0 . In other words, we simply shift $x_3 \rightarrow x_3 + r_0$, which yields

$$G_{\mathbf{k}_\perp}(x_3, r_0) = -2\pi i \alpha \cos \phi e^{-k_\perp x_3} e^{-k_\perp r_0}. \quad (\text{A5})$$

Appendix B: Analytic form of the spectrum for homogeneous isotropic NN in the frozen approximation

In this appendix, we derive the analytic results for the spectrum (18) for HI turbulence in the frozen approximation. We start from Eq. (18)

$$S_g^{ft} = \frac{\mathcal{E}_T}{\mathcal{E}^{1/3}} \int \frac{d^3 \mathbf{k}}{(2\pi)^2} k^{-11/3} |G_{\mathbf{k}}(r_0)|^2 \delta(\omega - \mathbf{k} \cdot \mathbf{U}). \quad (\text{B1})$$

To compute the integral, first, we choose the geometry illustrated in Fig. 1, and we adopt a cartesian set of coordinates in the integrated variable \mathbf{k} . Moreover, we choose the wind speed to be parallel to the earth's surface. This simplifies the calculations since

$$\mathbf{k} \cdot \mathbf{U} = k_\perp U \cos(\phi - \psi), \quad (\text{B2})$$

where U is the wind speed and $k_\perp = \sqrt{k_1^2 + k_2^2}$. To get rid of the angle ψ in the Dirac delta, we rotate the reference frame around the k_3 -axis by an angle ψ and we write $\cos \phi = k_1/k_\perp$. Then, using Eq. (A3) we get

$$\begin{aligned} S_g^{ft} &= \frac{\mathcal{E}_T}{(2\pi)^2 \mathcal{E}^{1/3}} \int_0^\infty d^3 \mathbf{k} k^{-11/3} |G_{\mathbf{k}}|^2 \delta(\omega - k_1 U) \\ &= \alpha^2 \frac{\mathcal{E}_T}{\mathcal{E}^{1/3}} \int_{-\infty}^\infty dk_1 \int_{-\infty}^\infty dk_2 \int_{-\infty}^\infty dk_3 \\ &\quad \times k^{-17/3} k_\perp^{-2} (k_1^2 \cos^2 \psi + k_2^2 \sin^2 \psi) \\ &\quad \times \delta(\omega - k_1 U) e^{-2k_\perp r_0}. \end{aligned} \quad (\text{B3})$$

The integral over k_3 can be easily done and yields

$$\int_{-\infty}^\infty \frac{dk_3}{k^{17/3}} = \sqrt{\pi} \frac{\Gamma(7/3)}{\Gamma(17/6)} k_\perp^{-14/3}. \quad (\text{B4})$$

The integral over k_1 is instead trivial using the delta function, which simply sets $k_1 = \omega/U$.

The last integration in k_2 can be solved changing the integration variable, mapping $k_2 \rightarrow \xi = \sqrt{1 + (U k_2/\omega)^2}$. With this substitution, the integral becomes

$$\begin{aligned} S_g^{ft} &= 2\mathcal{C} \int_1^\infty d\xi \frac{\xi}{\sqrt{\xi^2 - 1}} \\ &\quad \times \frac{\cos^2 \psi + (\xi^2 - 1) \sin^2 \psi}{\xi^{20/3}} e^{-2\omega r_0 \xi/U}, \end{aligned} \quad (\text{B5})$$

where $\mathcal{C} = \alpha^2 \mathcal{E}_T \sqrt{\pi} \Gamma(7/3)/(\mathcal{E}^{1/3} \Gamma(17/6)) U^{8/3} \omega^{-11/3}$. The integral can be done analytically and gives a combination of hypergeometric functions

$$\begin{aligned}
S_g^{ft} = & 2\mathcal{C} \cos^2 \psi \left\{ \frac{\sqrt{\pi} \Gamma\left(\frac{17}{6}\right) {}_1F_2\left(-\frac{7}{3}; -\frac{11}{6}, \frac{1}{2}; x^2\right)}{2\Gamma\left(\frac{10}{3}\right)} + 32x\Gamma\left(-\frac{17}{3}\right) \right. \\
& \times \left[2^{2/3} x^{14/3} {}_1F_2\left(\frac{1}{2}; \frac{10}{3}, \frac{23}{6}; x^2\right) - \frac{26180\sqrt{\pi} {}_1F_2\left(-\frac{11}{6}; -\frac{4}{3}, \frac{3}{2}; x^2\right)}{6561\Gamma\left(\frac{17}{6}\right)} \right] \Big\} \\
& + 2\mathcal{C} \sin^2 \psi \left\{ \frac{\sqrt{\pi} \Gamma\left(\frac{11}{6}\right) {}_1F_2\left(-\frac{7}{3}; -\frac{5}{6}, \frac{1}{2}; x^2\right)}{4\Gamma\left(\frac{10}{3}\right)} + 8x\Gamma\left(-\frac{11}{3}\right) \right. \\
& \times \left[2^{2/3} x^{8/3} {}_1F_2\left(-\frac{1}{2}; \frac{7}{3}, \frac{17}{6}; x^2\right) - \frac{55\sqrt{\pi} {}_1F_2\left(-\frac{11}{6}; -\frac{1}{3}, \frac{3}{2}; x^2\right)}{243\Gamma\left(\frac{17}{6}\right)} \right] \Big\}, \tag{B6}
\end{aligned}$$

where, for convenience, we defined $x \equiv r_0\omega/U$.

Appendix C: Asymptotic results in homogeneous isotropic turbulence

1. Frozen turbulence

An explicit expression for the dimensionless spectrum \hat{S}_g^{ft} in Eq. (19) is obtained by substituting Eq. (A3) into Eq. (18). Let us set $\mathbf{U} = (U, 0, 0)$ and introduce dimensionless quantities $\hat{\omega} = \omega r_0/U$ and $\hat{k} = kU/\omega$. We find

$$\hat{S}_g^{ft} = \int \frac{d\hat{k}_2 d\hat{k}_3}{\hat{k}^{17/3}} \cos^2(\psi + \phi) e^{-2\hat{k}_\perp \hat{\omega}} \tag{C1}$$

where $\hat{k}_1 = 1$ from the Dirac delta in Eq. (18). We easily verify that the integral converges to a finite function of ψ for $\hat{\omega} \rightarrow 0$. This implies that for $\omega \ll U/r_0$, S_g scales like a power in ω and U (see Eq. (19)).

In the opposite limit $r_0 \gg U/\omega$, we can approximate

$$\begin{aligned}
\hat{S}_g^{ft} \simeq & \int \frac{d\hat{k}_2 d\hat{k}_3}{\hat{k}^{17/3}} \left[\frac{\cos^2 \psi + \hat{k}_2^2 \sin^2 \psi}{1 + \hat{k}_2^2} \right] \\
& \times \exp \left[-\hat{\omega}(2 + \hat{k}_2^2) \right], \tag{C2}
\end{aligned}$$

where we have exploited $\hat{k}_2 \sim \hat{\omega}^{-1/2} \ll 1$. Evaluating the integral in Eq. (C2) to lowest order in $\hat{\omega}^{-1}$ yields Eq. (20).

2. Weak wind regime

Let us indicate $p = k_\perp/k$. We can evaluate the integral in Eq. (15) in spherical coordinates. If $h[\tau_k(\omega - \mathbf{k} \cdot \mathbf{U})] \simeq h(\tau_k \omega)$, the integral over ϕ in Eq. (15) is trivial, so that

we are left with

$$\begin{aligned}
S_g^{ww} & \sim \frac{\mathcal{E}_T \alpha^2}{\mathcal{E}^{1/3}} \int_0^{+\infty} dk k^{-13/3} h(\tau_k \omega) \int_0^1 dp p e^{-2pkr_0} \\
& = \frac{\mathcal{E}_T \alpha^2}{\mathcal{E}^{1/3}} \int_0^{+\infty} dk \frac{1 - (1 + 2kr_0)e^{-2kr_0}}{4k^{19/3} r_0^2} h(\tau_k \omega) \\
& \sim \frac{\mathcal{E}_T \alpha^2}{\mathcal{E}^{1/3}} \int_{k_\omega}^{+\infty} dk \frac{1 - (1 + 2kr_0)e^{-2kr_0}}{k^{19/3} r_0^2}, \tag{C3}
\end{aligned}$$

where k_ω is defined in Eq. (22). We can now carry out the integral in Eq. (C3) in the two limits of large and small depth and we recover Eq. (21).

Appendix D: Time correlations for turbulence in the surface layer

Let us indicate

$$\eta = \omega \tau_k(\bar{x}_3), \quad \zeta = k_\perp \tau_k(\bar{x}_3) U_{\bar{x}_3}. \tag{D1}$$

We find the following limit behaviors for the function A in Eq. (27):

- If either $\zeta \ll \eta \sim 1$ or $\eta \gg 1$ and $\zeta \ll |h(\eta - \zeta)/h'(\eta - \zeta)|$,

$$A(\eta, \zeta) \simeq \pi h(\eta). \tag{D2}$$

- If either $\zeta \gg \max(\eta, 1)$ or $\zeta > \eta \gg 1$,

$$A(\eta, \zeta) \sim \frac{\cos^2(\psi + \phi_m)}{\zeta \sin \phi_m}, \tag{D3}$$

where $\phi_m = \arccos(\eta/\zeta)$.

- If $\eta \gg \max(1, \zeta)$ and $\zeta \gg |h(\eta - \zeta)/h'(\eta - \zeta)|$,

$$A(\eta, \zeta) \sim \cos^2 \psi \frac{h^{3/2}(\eta - \zeta)}{|\zeta h'(\eta - \zeta)|^{1/2}}. \tag{D4}$$

The result in Eq. (D2) is straightforward. The result in Eq. (D3) is obtained by saddle-point approximation, expanding $h(\eta - \zeta \cos \phi) \simeq h(\zeta \phi' \sin \phi_m)$, $\phi' = \phi - \phi_m$,

where $\phi_m = \arccos(\eta/\zeta)$, and then integrating from $-(\zeta \sin \phi_m)^{-1}$ to $(\zeta \sin \phi_m)^{-1}$. The result in Eq. (D4) is obtained by expanding

$$\begin{aligned} h(\eta - \zeta \cos \phi) &\simeq h(\eta - \zeta(1 - \phi^2/2)) \\ &\simeq h(\eta - \zeta) + (\zeta \phi^2/2)h'(\eta - \zeta) \end{aligned}$$

and then integrating by steepest descent. In order to have $\hat{A} = O(1)$, it is sufficient that $\eta \sim \zeta \sim 1$.

Appendix E: Asymptotic results for turbulence in the surface layer

In the integral in Eq. (26) we separate contributions from integral scale vortices (“domain 1”, $k\bar{x}_3 < 1$) and those from inertial scale vortices (“domain 2”, $k\bar{x}_3 > 1$). Different cutoffs act in the integral:

- The term e^{-2kpro} , accounting for the decay of the signal with the depth of the detector;
- The factor $k^{-13/3}$, associated with the decay of turbulent fluctuations at small scales;
- The function A that filters eddies at time-scales below ω^{-1} .

The analysis in Appendix D tells us that the function A is surely negligible for $\eta \gg \max(1, \zeta)$. Let us analyze the remaining regions $\eta < 1$ and $\zeta > \eta > 1$.

The region $\zeta > \eta > 1$ corresponds in domain 1 to

$$\begin{aligned} \hat{\omega}\hat{x}_3 &< \frac{\hat{k}_\perp\hat{x}_3}{\kappa} \ln(e\hat{x}_3) < \frac{1}{\kappa} \ln(e\hat{x}_3) \\ &\Rightarrow 1 > \hat{k}\hat{x}_3 > \frac{\kappa\hat{\omega}\hat{x}_3}{\ln(e\hat{x}_3)} \\ &\Rightarrow \hat{\omega} < \frac{\ln(e\hat{x}_3)}{\kappa\hat{x}_3} < \frac{1}{\kappa}, \end{aligned} \quad (\text{E1})$$

where $\hat{x}_3 = \bar{x}_3/z_0$. The region $\eta < 1$ with $\hat{x}_3 > 1$, in turn, corresponds to $\hat{\omega} < 1$. We thus reach the conclusion that for $\hat{\omega}$ sufficiently large ($\hat{\omega} \gtrsim 2.5$), integral range vortices do not contribute to \hat{S}_g .

1. Large frequency limit

The large $\hat{\omega}$ limit confines us to domain 2. The region $1 < \eta < \zeta$ corresponds to

$$\begin{aligned} \hat{\omega} &< \frac{p\hat{k}}{\kappa} \ln(e\hat{x}_3) < \frac{\hat{k}}{\kappa} \ln(e\hat{x}_3) \\ &\Rightarrow \hat{k} > \frac{\kappa\hat{\omega}}{\ln(e\hat{x}_3)}, \end{aligned} \quad (\text{E2})$$

and the integral in p in Eq. (26) is bounded in this range by

$$p > p_{\min} = \frac{\kappa}{\hat{k}^{2/3} \ln(e\hat{x}_3)}. \quad (\text{E3})$$

Now, unless the detector is at the surface, the term \hat{r}_0 is large, and thus, unless $p \simeq 0$, the factor $e^{-2p\hat{k}\hat{r}_0}$ in Eq. (26) is going to be very small. The contribution to \hat{S}_g from the region $\zeta > \eta > 1$ is in this case exponentially damped.

To get $p_{\min} = 0$ we need to go to the region $\eta < 1$, corresponding to the condition on k :

$$\hat{k} > \hat{k}_{\min} \simeq \hat{\omega}^{3/2} \hat{x}_3^{1/2}. \quad (\text{E4})$$

The function B (28) is $O(1)$ in the whole integration domain of Eq. (26), and we thus get

$$\hat{S}_g \sim \int_1^{+\infty} \hat{x}_3^{-4/3} d\hat{x}_3 \int_{\hat{k}_{\min}}^{+\infty} \hat{k}^{-13/3} d\hat{k} \int_0^1 p dp e^{-2p\hat{k}\hat{r}_0} \sim \hat{\omega}^{-8} \hat{r}_0^{-2}. \quad (\text{E5})$$

2. Small frequency limit

Let us consider first domain 1. The two conditions $\eta < 1$ and $\bar{x}_3 < L_O$ imply

$$\hat{x}_3 < \hat{x}_{3,\max} = \min(\hat{\omega}^{-1}, \hat{L}_O). \quad (\text{E6})$$

The contribution to \hat{S}_g from domain 1 is therefore

$$\hat{S}_{g1} \sim \int_{\hat{x}_{3,\min}}^{\hat{x}_{3,\max}} d\hat{x}_3 \int_0^{1/\hat{x}_3} d\hat{k} \int_0^1 dp g_1(p, \hat{k}, \hat{x}_3),$$

where $g_1(p, \hat{k}, \hat{x}_3) = pB\hat{x}_3 e^{-2p\hat{k}\hat{r}_0}$. The integral is concentrated at $(\hat{x}_3, \hat{k}) \sim (\hat{x}_{3,\max}, 0)$. We find the limit be-

haviors

$$\hat{S}_{g1} \sim \begin{cases} \hat{x}_{3,\max}^3, & \hat{r}_0 \lesssim \hat{x}_{3,\max} \\ \hat{x}_{3,\max}^5 \hat{r}_0^{-2}, & \hat{r}_0 \gg x_{3,\max} \end{cases} \quad (\text{E7})$$

Let us switch to domain 2 and continue to focus on the region $\eta < 1$, for which $A \sim 1$. We have now

$$\hat{S}_{g2} \sim \int_{\hat{x}_{3,\min}}^{\hat{x}_{3,\max}} d\hat{x}_3 \int_{1/\hat{x}_3}^{+\infty} d\hat{k} \int_0^1 dp g_2(p, \hat{k}, \hat{x}_3),$$

where $g_2(p, \hat{k}, \hat{x}_3) = pB\hat{k}^{-13/3}\hat{x}_3^{-4/3}e^{-2p\hat{k}\hat{r}_0}$. In this case the integral is concentrated at $(\hat{x}_3, \hat{k}) \sim (\hat{x}_{3,\max}, 1/\hat{x}_{3,\max})$. We can verify that $\hat{S}_{g2} \sim \hat{S}_{g1}$, and thus recover Eqs. (32) and (33).

Appendix F: General scaling of the noise spectra with r_0

In Section IV and Section V we have shown that, in some limiting cases S_g scales as $1/r_0^2$ (see Eqs. (21), (31) and (32)). Here we prove that such a behavior generally arises whenever vortex decay dominates over wind advection and the detector depth is sufficiently large, independently of the chosen turbulence model. From Eqs. (15) and (26), we can see that S_g can be expressed in the general form

$$S_g \sim \int_0^1 dp \frac{p}{\sqrt{1-p^2}} \int_{x_{\min}}^L dx \int_0^{2\pi} d\phi \cos^2 \phi \quad (\text{F1}) \\ \times \int_0^\infty dk f(p, x, \phi, k) h[\tau_k(\omega - p \cos \phi k U)] F(pk r_0).$$

Here f is the spatial part of the correlation functions, h contains information about time correlations and F is a function whose form depend on the chosen geometry. In particular, $F(pk r_0) = e^{-2pk r_0}$ in our case. We assume that:

- The integral (F1) is convergent, which is always the case for reasonable models;
- The function h satisfies the properties given in Section IV below Eq. (14), i.e. $h(z)$ has a maximum for $z = 0$ and $h(z) \rightarrow 0$ at least exponentially for $z \rightarrow \infty$;
- f is regular over the whole integration domain;
- $F(pk r_0) \rightarrow 0$ for $pk r_0 \gg 1$ sufficiently fast (at least exponentially).

Due to the properties of h , we see that the contribution to the integral over k in Eq. (F1) will be peaked around some value $k = \bar{k}$, whose specific value depends on the other parameters and on the specific model. Thus

$$S_g \sim \int_0^1 dp \frac{p}{\sqrt{1-p^2}} \int_{x_{\min}}^L dx \int_0^{2\pi} d\phi \cos^2 \phi \quad (\text{F2}) \\ \times \bar{k} f(p, x, \phi, \bar{k}) h[\tau_{\bar{k}}(\omega - p \cos \phi \bar{k} U)] F(p \bar{k} r_0).$$

If we now assume $\omega \gg \bar{k} U$, i.e. vortex decay dominates over wind advection, we see that the function h will become independent of the wind speed. One can now perform the integrals over x and ϕ , so that

$$S_g \sim \bar{k} h(\tau_{\bar{k}} \omega) \int_0^1 dp \frac{p}{\sqrt{1-p^2}} \quad (\text{F3}) \\ \times g(p, x_{\min}, L, \bar{k}) F(p \bar{k} r_0).$$

When $r_0 \gg 1/\bar{k}$, we see that the only non-negligible contribution to the integral comes from the values of $p \lesssim 1/(\bar{k} r_0) \ll 1$, according to the last assumption above. The integral becomes then

$$S_g \sim \bar{k} h(\tau_{\bar{k}} \omega) g(0, x_{\min}, L, \bar{k}) F(0) \int_0^{1/(\bar{k} r_0)} dp p \quad (\text{F4}) \\ \sim \frac{h(\tau_{\bar{k}} \omega) g(0, x_{\min}, L, \bar{k}) F(0)}{\bar{k} r_0^2}.$$

[1] B. P. Abbott *et al.* (LIGO Scientific, Virgo), Phys. Rev. Lett. **116**, 061102 (2016), arXiv:1602.03837 [gr-qc].

[2] F. Acernese *et al.* (VIRGO), Class. Quant. Grav. **32**, 024001 (2015), arXiv:1408.3978 [gr-qc].

[3] B. P. Abbott *et al.* (LIGO Scientific, Virgo), Phys. Rev. Lett. **116**, 241103 (2016), arXiv:1606.04855 [gr-qc].

[4] B. P. Abbott *et al.* (LIGO Scientific, Virgo), Phys. Rev. Lett. **119**, 161101 (2017), arXiv:1710.05832 [gr-qc].

[5] B. P. Abbott *et al.* (LIGO Scientific, Virgo, Fermi GBM, INTEGRAL, IceCube, AstroSat Cadmium Zinc Telluride Imager Team, IPN, Insight-Hxmt, ANTARES, Swift, AGILE Team, 1M2H Team, Dark Energy Camera GW-EM, DES, DLT40, GRAWITA, Fermi-LAT, ATCA, ASKAP, Las Cumbres Observatory Group, OzGrav, DWF (Deeper Wider Faster Pro-

gram), AST3, CAASTRO, VINROUGE, MASTER, J-GEM, GROWTH, JAGWAR, CaltechNRAO, TTU-NRAO, NuSTAR, Pan-STARRS, MAXI Team, TZAC Consortium, KU, Nordic Optical Telescope, ePESSTO, GROND, Texas Tech University, SALT Group, TOROS, BOOTES, MWA, CALET, IKI-GW Follow-up, H.E.S.S., LOFAR, LWA, HAWC, Pierre Auger, ALMA, Euro VLBI Team, Pi of Sky, Chandra Team at McGill University, DFN, ATLAS Telescopes, High Time Resolution Universe Survey, RIMAS, RATIR, SKA South Africa/MeerKAT), Astrophys. J. Lett. **848**, L12 (2017), arXiv:1710.05833 [astro-ph.HE].

[6] B. P. Abbott *et al.* (LIGO Scientific, Virgo, Fermi-GBM, INTEGRAL), Astrophys. J. Lett. **848**, L13 (2017), arXiv:1710.05834 [astro-ph.HE].

- [7] B. P. Abbott *et al.* (LIGO Scientific, Virgo), Phys. Rev. Lett. **116**, 221101 (2016), [Erratum: Phys.Rev.Lett. 121, 129902 (2018)], arXiv:1602.03841 [gr-qc].
- [8] B. P. Abbott *et al.* (LIGO Scientific, Virgo), Phys. Rev. D **100**, 104036 (2019), arXiv:1903.04467 [gr-qc].
- [9] R. Abbott *et al.* (LIGO Scientific, Virgo), Phys. Rev. X **11**, 021053 (2021), arXiv:2010.14527 [gr-qc].
- [10] R. Abbott *et al.* (LIGO Scientific, KAGRA, VIRGO), Astrophys. J. Lett. **915**, L5 (2021), arXiv:2106.15163 [astro-ph.HE].
- [11] K. Somiya (KAGRA), Class. Quant. Grav. **29**, 124007 (2012), arXiv:1111.7185 [gr-qc].
- [12] B. P. Abbott *et al.* (KAGRA, LIGO Scientific, Virgo, VIRGO), Living Rev. Rel. **21**, 3 (2018), arXiv:1304.0670 [gr-qc].
- [13] T. Akutsu *et al.* (KAGRA), PTEP **2021**, 05A101 (2021), arXiv:2005.05574 [physics.ins-det].
- [14] M. Punturo *et al.*, Class. Quant. Grav. **27**, 194002 (2010).
- [15] B. P. Abbott *et al.* (LIGO Scientific), Class. Quant. Grav. **34**, 044001 (2017), arXiv:1607.08697 [astro-ph.IM].
- [16] B. Sathyaprakash *et al.*, Class. Quant. Grav. **29**, 124013 (2012), [Erratum: Class.Quant.Grav. 30, 079501 (2013)], arXiv:1206.0331 [gr-qc].
- [17] M. Maggiore *et al.*, JCAP **03**, 050 (2020), arXiv:1912.02622 [astro-ph.CO].
- [18] J. Harms, Living Reviews in Relativity **22**, 6 (2019).
- [19] J. Harms, L. Naticchioni, E. Calloni, R. De Rosa, F. Ricci, and D. D’Urso, (2022), arXiv:2202.12841 [gr-qc].
- [20] P. R. Saulson, Phys. Rev. D **30**, 732 (1984).
- [21] T. Creighton, Class. Quant. Grav. **25**, 125011 (2008), arXiv:gr-qc/0007050.
- [22] C. Cafaro and S. A. Ali, (2009), arXiv:0906.4844 [gr-qc].
- [23] R. B. Stull, *An introduction to boundary layer meteorology*, Vol. 13 (Springer Science & Business Media, 1988).
- [24] H. Schlichting and K. Gersten, *Boundary-layer theory* (Springer Science & Business Media, 2003).
- [25] I. Troen and E. Lundtang Petersen, *European Wind Atlas* (Risø National Laboratory, 1989).
- [26] A. Obukhov, Boundary-Layer Meteorology **2**, 7 (1971).
- [27] A. N. Kolmogorov, Proceedings of the Royal Society of London. Series A: Mathematical and Physical Sciences **434**, 9 (1991).
- [28] V. Belinicher and V. L’vov, Sov. Phys. JETP **66**, 303 (1987).
- [29] T. Wu and G. He, Physical Review Fluids **6**, 054602 (2021).
- [30] A. Naguib and C. Wark, Journal of Fluid Mechanics **243**, 541 (1992).
- [31] “AtmosphericNN GitHub repository,” <https://github.com/maurooi/AtmosphericNN> (2022).
- [32] G. Peter Lepage, Journal of Computational Physics **27**, 192 (1978).
- [33] A. A. Alves Junior, “Multithreadcorner/hydra,” (2018).
- [34] R. Stoll, J. A. Gibbs, S. T. Salesky, W. Anderson, and M. Calaf, Boundary-Layer Meteorology **177**, 541 (2020).